Biophysical Journal
Article

Biophysical Society

Location of dopamine in lipid bilayers and its relevance to neuromodulator function

Azam Shafieenezhad,[1] Saheli Mitra,[2] Stephen R. Wassall,[1] Stephanie Tristram-Nagle,[2] John F. Nagle,[2] and Horia I. Petrache[1,*]

[1]Department of Physics, Indiana University Purdue University Indianapolis, Indianapolis, Indiana and [2]Department of Physics, Carnegie Mellon University, Pittsburgh, Pennsylvania

ABSTRACT Dopamine (DA) is a neurotransmitter that also acts as a neuromodulator, with both functions being essential to brain function. Here, we present the first experimental measurement of DA location in lipid bilayers using x-ray diffuse scattering, solid-state deuterium NMR, and electron paramagnetic resonance. We find that the association of DA with lipid headgroups as seen in electron density profiles leads to an increase of intermembrane repulsion most likely due to electrostatic charging. DA location in the lipid headgroup region also leads to an increase of the cross-sectional area per lipid without affecting the bending rigidity significantly. The order parameters measured by solid-state deuterium NMR decrease in the presence of DA for the acyl chains of PC and PS lipids, consistent with an increase in the area per lipid due to DA. Most importantly, these results support the hypothesis that three-dimensional diffusion of DA to target membranes could be followed by relatively more efficient two-dimensional diffusion to receptors within those membranes.

SIGNIFICANCE Knowing how dopamine interacts with lipid membranes is relevant to the understanding of transmission and modulation processes. Our experimental results show that dopamine has high affinity for the lipid headgroup region even in the absence of specialized receptors. This suggests that dopamine may first be collected by the target axon membrane and then diffuse along that membrane to its receptors that modulate function.

INTRODUCTION

Dopamine (DA) is a neurotransmitter and neuromodulator (1). There are several DA pathways in the brain that play major roles in reward-motivated behavior, motor control, and release of various hormones. DA deficiency and abnormalities in DA signaling can cause life-impairing diseases including Parkinson's, attention deficit hyperactivity disorder, and schizophrenia (2,3). DA has been extensively studied in biological processes, including its role against ferroptosis in cells (4), molecular transport (5,6), interaction with receptors and transporters (7–9), and ion transfer (10).

As a neuromodulator, DA performs its function by diffusing from the release site to G protein-coupled receptors distributed over micrometer length scales (1,11,12). While aliphatic neurotransmitters such as acetylcholine, GABA, aspartate, glutamate, glycine, and serine might interact directly with their target proteins (13), neurotransmitters that contain aromatic groups such as DA, L-dopa, epinephrine, norepinephrine, adenosine, melatonin (14), serotonin (15–17), and histamine have an affinity to lipid headgroups (18) and therefore have a more complex mode of action that involve a broader range of spatial and temporal scales (1).

The conventional understanding is that DA undergoes three-dimensional diffusion through aqueous spaces in order to activate both local and distant G protein-coupled receptors (1,13). Then, the membrane and its lipid composition would play no role. An alternative would be that the membrane acts as a collector of DA, concentrating it in the membrane to provide two-dimensional diffusion to receptors that could be more efficient than purely three-dimensional diffusion. In support, phospholipids make a difference in the process of synaptic neurotransmission and neuromodulation (19–21). Our results support this alternative.

Knowledge on the effect of DA on model lipid membranes has accumulated from calorimetry methods (2),

Submitted August 24, 2022, and accepted for publication February 13, 2023.

*Correspondence: hpetrach@iupui.edu

Azam Shafieenezhad's present address is Department of Neuroscience, The University of Texas at Austin, Austin, Texas

Editor: Michael F. Brown.

https://doi.org/10.1016/j.bpj.2023.02.016

solution-state NMR (22), and, more recently, vibrational sum frequency generation spectroscopy (21,23). Additionally, it has been shown that DA decreases the main transition temperature of negatively charged lipid membranes (2) and that it breaks the peroxidation chain of methyl linoleate in liposomes assembled from neutral and negatively charged phospholipids (24). The emerging picture of DA interaction with lipid membranes may benefit from a more direct experimental measurement of the location of DA in lipid bilayers and of its effect on membrane structure and interactions. In this work, we use a combination of complementary experimental methods that include x-ray diffuse scattering (XDS), solid-state NMR, and electron paramagnetic resonance (EPR). From XDS we learn 1) where DA resides in the membrane, 2) how DA affects mechanical properties of membranes, in particular the bending rigidity K_C, and 3) how the bilayer structure is affected. The bending rigidity K_C is a material parameter of lipid membranes that sets the energy scale for membrane shape deformations. Membrane curvature deformations are implicated in the function of membrane receptors and ion channels (25) and affect interactions between membranes, which are relevant to cellular processes such as membrane fusion (26–29). In addition to providing information about the effect of DA on the bilayer, XDS provides the compression modulus B that quantifies the interaction between bilayers (30–33). Solid-state ^{2}H NMR focuses on how much DA affects the hydrocarbon region of the bilayer by providing order parameter profiles. From EPR measurements, we obtain rotational correlation times of paramagnetic probe additives that confer information on the location of DA and on local membrane viscosity.

The interaction and dynamics of DA (and related neurotransmitters) are receiving sustained attention from molecular dynamics (MD) simulations (6,7,15,18). Such approaches have the obvious advantage that information is obtained at atomic detail and at timescales ranging from picoseconds to microseconds or more. However, these highly detailed results are subject to uncertainties due to the choice of force fields. Therefore, experimental data in terms of electron density profiles, order parameters, and correlation times as reported in this work can provide a test for MD simulations and guide future developments.

MATERIALS AND METHODS

Materials

1,2-dioleoyl-*sn*-glycero-3-phosphocholine (DOPC), 1,2-dilauroyl-*sn*-glycero-3-phosphocholine (DLPC), 1,2-dioleoyl-*sn*-glycero-3-phospho-L-serine (sodium salt) (DOPS), 1-palmitoyl-d_{31}-2-oleoyl-*sn*-glycero-3-phosphocholine (POPC-d_{31}), 1-palmitoyl-d_{31}-2-oleoyl-*sn*-glycero-3-phospho-L-serine (sodium salt) (POPS-d_{31}), and N-tempoyl palmitamide (N-TEMPO) were purchased from Avanti Polar Lipids (Alabaster, AL, USA). DA hydrochloride and 16-doxyl-stearic acid (16-DSA) were purchased from Sigma-Aldrich (St. Louis, MO, USA).

X-ray

X-ray sample preparation

DOPC and DLPC lipids were separately dissolved in chloroform to make 20 mg/mL stock solutions. Similarly, a 20 mg/mL solution of DA was prepared in methanol. Appropriate volumes of lipid and DA stock solutions were mixed to obtain a final volume of 200 μL containing a 4 mg mixture of lipid and DA in molar ratios 0:1, 1:10, and 1:3 (DA:lipid). Samples were spread on flat acid-cleaned silicon wafers ($30 \times 15 \times 1$ mm^3) and dried under the fume hood using the rock and roll procedure to make a thin film of oriented multilamellar samples (34,35). Finally, samples were kept in a vacuum oven for at least 2 h to remove the last traces of solvent. Dried samples were trimmed to form a 5 mm strip in the center of the wafer, parallel to the 30 mm edge. They were brought to full hydration through the vapor in a thick-walled hydration chamber with a Peltier cooler under the wafer to gently condense water into the sample.

X-ray scattering

The x-ray wavelength was 1.5418 Å. The x-ray beam impinges into a horizontally held sample while the silicon wafer is rotated constantly between $\theta_{\min} = -1.6^\circ$ and $\theta_{\max} = 7^\circ$ at 20° per second during data collection. Background scattering was collected with the angle θ set to -2.4°. Data were collected using a Rigaku (The Woodlands, TX, USA) mercury charge-coupled device with a 1024×1024 pixel array. The distance between charge-coupled device and sample center was 287 mm. Measurements were carried out at 25°C.

X-ray data analysis

X-ray data were analyzed using the NFIT program (36–38). The light background was subtracted, and a two-box subtraction was applied in order to interpolate the lateral background under the actual data. Repeat lattice spacing D was measured using $h = 1, 2$ lamellar peaks. The bending modulus K_C and compression modulus B were calculated using three different fitting boxes, $q_{r2} = q_{r1} + 150$, 200, or 300 for lobes 2 and 3, where $q_{r1} = q_{r0} + 11$ and q_{r0} is the pixel position of the specular center. The molecular volume of DA (246 Å^3) has been obtained by first measuring the DA density using a Mettler Toledo DE45 density meter and has been used in electron density profile analysis. Structural analysis was performed using the Scattering Density Profile (SDP) computer program, where form factor data derived from the XDS intensity data and molecular volumes are inputs (39).

Mean-square fluctuations

The statistical average of out-of-plane excursions of membranes due to shape fluctuations is a function of K_C, B, and temperature, given by

$$\sigma^2 = \frac{k_B T}{2\pi} \frac{1}{\sqrt{K_C B}}. \qquad \text{(Equation 1)}$$

For completeness, the free energy per unit area is given by

$$F = F_{bare} + \frac{k_B T}{2\pi}\sqrt{\frac{B}{K_C}} = F_{bare} + \left(\frac{k_B T}{2\pi}\right)^2 \frac{1}{K_C \sigma^2}, \qquad \text{(Equation 2)}$$

where F_{bare} is the free energy in the absence of fluctuations and can be thought as the limit $K_C \to \infty$ and $B \to \infty$ with the constraint $B/K_C \to 0$ (30).

^{2}H NMR

^{2}H NMR sample preparation

20 mg POPC-d_{31} and 20 mg POPS-d_{31} were dried separately from chloroform solutions under a stream of nitrogen gas and then kept in the

lyophilizer to remove the remaining traces of chloroform. The dry powder was then hydrated to 50 wt % with DA solution in deuterium-depleted water in a molar ratio of 1:10 DA to lipid. The samples were vortexed and put through 5 cycles of freezing and thawing. Finally, the resultant suspensions were transferred to a 5 mm NMR tube that was sealed with a Teflon-coated plug. Sealed samples were stored at $-$ 80°C and equilibrated at room temperature before the measurements.

^{2}H NMR spectroscopy

Solid-state ^{2}H NMR spectra were recorded at 76.77 MHz on a homebuilt NMR spectrometer (40) reconfigured to operate with a wideline probe constructed by Doty Scientific (Columbia, SC, USA) in an 11.75 T superconducting magnet (Oxford Instruments, Osney Mead, UK). Pulse programming was achieved with an in-house assembled programmable generator (41), while signals were collected in quadrature by a dual-channel digital oscilloscope (R1200 M; Rapid Systems, Seattle, WA, USA). A phase-alternated quadrupolar echo sequence (90°_x-τ-90°_y-acquire-delay) was employed (42). The parameters used were 90° pulse width = 6 μs; separation between pulses τ = 50 μs; delay between pulse sequences = 1 s; sweep width = $\pm$250 kHz; and number of scans = 4096 or 8192. Temperature was maintained to $\pm$ 0.5°C by a Varian high-stability variable temperature controller.

^{2}H NMR spectra analysis

^{2}H NMR spectra obtained with lipid samples in the lamellar liquid crystalline phase are a superposition of doublets due to bilayers at all angles relative to the magnetic field (B). The splitting of the doublets is given by

$$\Delta\nu(\theta_{NB}) = \frac{3}{2}\left(\frac{e^2qQ}{h}\right)|S_{CD}|P_2(\cos\theta_{NB}). \quad \text{(Equation 3)}$$

In this equation, (e^2qQ/h) = 167 kHz is the quadrupole coupling constant, the angle θ_{NB} is the orientation of the membrane normal (N) with respect to the magnetic field direction, $P_2(\cos\theta_{NB})$ is the second-order Legendre polynomial, and S_{CD} is the CD bond order parameter (43). The splittings for carbon segments ($i = 2-16$) along a lipid chain were determined from the doublets resolved in de-Paked spectra ($\theta_{NB} = 0^\circ$) and used to construct profiles of $S_{CD}^{(i)}$ assuming monotonic variation (44–46).

EPR

EPR sample preparation

EPR samples were prepared using N-TEMPO to probe the headgroup region or 16-DSA to probe the chain region for three different lipids: DOPC, DLPC, and DOPS. First, a total of 20 mg lipid and EPR probe were mixed in chloroform separately for each lipid. The chloroform was then evaporated under a gentle stream of nitrogen gas. Remaining chloroform traces were removed during lyophilization. The resulting powder was hydrated with DA solutions to a concentration of 5 wt % lipid. The samples were mixed using a vortex mixer and 5 cycles of freezing and thawing. The molar ratio of DA to lipid and N-TEMPO was 50:500:1, and the ratio of DA to lipid and 16-DSA was 10:100:1.

EPR spectroscopy

EPR spectra were recorded at 9.29 GHz on a Bruker X-band ESP 300 EPR spectrometer (Billerica, MA, USA). Signals were detected as the first derivative of the absorption. The spectral parameters were microwave power = 12.6 mW; field center = 3305 G; sweep width = 100 G; sweep time = 167.77 s; time constant = 655.36 ms; modulation amplitude = 2 G; and data set = 2048 points. Experiments were run at 25°C.

EPR spectra analysis

For probes in quasi-isotropic motion, the EPR spectra can be used to calculate a rotational correlation time τ_c according to

$$\tau_c = 6.5\cdot10^{-10}W_0\left[\left(\frac{h_0}{h_{-1}}\right)^{1/2} - 1\right], \quad \text{(Equation 4)}$$

where W_0 is the distance between the central line of two peaks, h_0 is the height of the central field line, and h_{-1} is the height of the high field line (see Fig. S3). The prefactor $6.5\cdot10^{-10}$ s/G is an averaged parameter that depends on the anisotropic g value, anisotropic nitrogen hyperfine couplings, and the magnetic field strength (47,48).

RESULTS

Lamellar spacing, interaction parameters, and fluctuations

The effect of DA (Fig. 1) on the D-spacing of DOPC and DLPC multilamellar oriented samples is shown in Fig. 2. The figure also shows previous measurements in salt solutions, which provide reference swelling curves for these lipids (32). For both lipids, the D-spacing increases with added DA similarly to the effect of the monovalent KCl and KBr salts. The figure also shows that the effect of DA on the D-spacing is closer to that of KBr than to KCl, indicating that the DA effect is due to membrane charging similar to that of Br^- ions (31–33).

The bending modulus K_C and the compression modulus B obtained from the analysis of XDS data are plotted in Fig. 3. While the measured K_C values for DOPC are higher than for DLPC, DA does not have a major effect on K_C values for either lipid. The smaller K_C value for DLPC is consistent with its smaller membrane thickness compared with DOPC (49). As expected, the B parameter is a function of D. As mentioned in the introduction, the B parameter is an effective measure of the combined effect of intermembrane interactions, which are known to decrease with increasing

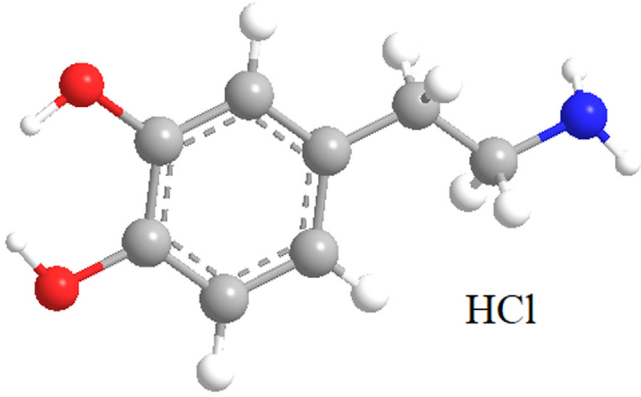

FIGURE 1 Chemical structure of dopamine (DA) hydrochloride using the standard CPK color codes: carbon (*gray*), oxygen (*red*), nitrogen (*blue*), and hydrogen (*white*). The chemical structure is drawn using ChemDraw. To see this figure in color, go online.

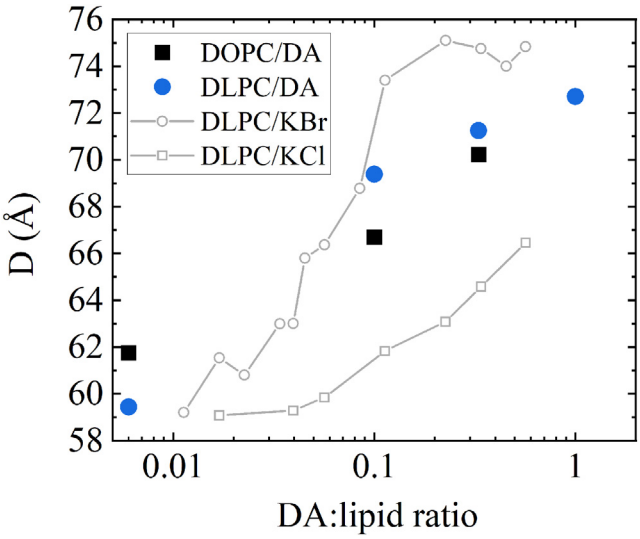

FIGURE 2 *D*-spacing versus DA:lipid molar ratio for DLPC and DOPC multilayers at 25°C. Data from DLPC in KCl and KBr salt solutions at corresponding salt:lipid molar ratios are also shown to provide reference swelling curves (32). To see this figure in color, go online.

distance. However, it is surprising that the B parameter for the two lipids appears to follow the same curve at higher D-spacing values.

The interlamellar spacing fluctuations σ of DOPC and DLPC as a function of D-spacing corresponding to different amounts of DA are presented in Fig. 4. These are calculated from the measured values of K_C and B according to Eq. 1. In the absence of DA, a higher value of σ is measured for DLPC compared with DOPC due to smaller K_C. With increasing DA concentration and, consequently, D-spacing, σ increases for both lipids due to the decrease of the compression parameter B.

A summary of parameters obtained from x-ray data of DOPC and DLPC for different molar ratios of DA to lipid is given in Table 1. Here, $2D_C$ is the hydrocarbon thickness, and D_B is the overall Luzzati bilayer thickness calculated using molecular volumes and the cross-sectional area per lipid (Fig. 5) obtained obtained from the SDP program. The thickness of each interfacial headgroup region is about 10 Å (50), so the thickness of the pure interlamellar water region D_W' is $D - 2D_C - 20$ Å.

Electron density profiles

Fig. 6 shows electron density profiles (EDPs) obtained from the analysis of XDS data using the SDP program. This analysis provides not only the overall density profiles but also the contribution of various lipid components, water, and DA. In particular, the DA location is indicated by the shaded distributions. Attempts to place DA at different locations, including in the interlamellar water region or in the hydrocarbon region, resulted in larger χ^2 values than the ones shown in Fig. 6.

In Table 2, we show the distance D_{peaks} between the peaks of the overall EDPs, the average position of DA in the bilayer z_{DA}, and the average position of DA with respect to the EDP peak on the righthand side of the bilayer. We find that DA resides deeper in the headgroup region in the case of DOPC bilayers compared with DLPC, possibly due to the lower lateral density (larger area per lipid) in the case of DOPC. Aside from this minor difference, the major finding is that DA has a high affinity for the interfacial, headgroup region of the lipid bilayer compared with either the hydrocarbon region or, most importantly, with the interlamellar, pure water region. Table 1 shows that the interlamellar thickness D_W' is as large as or larger than the two interfacial thicknesses (2 × 10 Å), so there is ample aqueous volume for the DA to reside in. Our result in Fig. 6 shows that DA has a much higher affinity for the interfacial region. While the undetectability of any DA in the interlamellar space precludes a quantitative determination of the partition coefficient of DA between water and the bilayer, it is clear that it is large. This is supported by surface plasmon resonance experiments as shown in the supporting material. However, our x-ray result is advantageous because it distinguishes between the hydrocarbon and the interfacial regions of the bilayer.

For ^{2}H NMR spectroscopy, we have used the common lipids POPC-d_{31} and POPS-d_{31}, which contain a deuterated

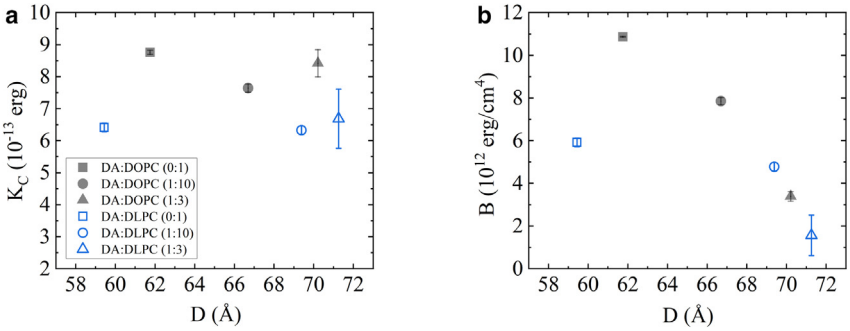

FIGURE 3 Bending and compression moduli obtained from XDS analysis. (*a*) The bending modulus K_C of DOPC and DLPC and (*b*) the corresponding compression modulus B as a function of D-spacing for various molar ratios of DA to lipid at 25°C. Measurements for each lipid/DA composition are from single samples. The average bending modulus K_C and compression modulus B were calculated using the NFIT program (see materials and methods) using three different fitting boxes, $q_{r2} = q_{r1} + 150$, 200, or 300, and error bars indicate the standard deviation from the mean. For some data points, the standard deviation bars are within the symbols. The K_C and B averages and errors are shown in Table 1. To see this figure in color, go online.

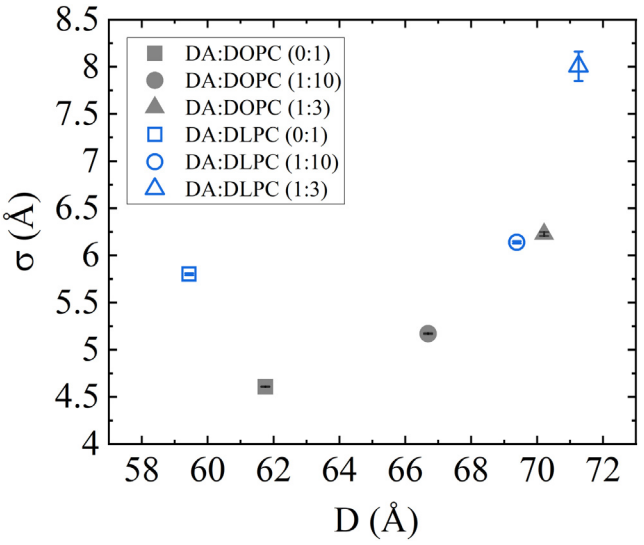

FIGURE 4 The interlamellar spacing fluctuations σ of DOPC and DLPC as a function of *D*-spacing corresponding to different molar ratios of DA to lipid at 25°C. The interlamellar spacing fluctuations σ were calculated using the average values of K_C and B, and errors are calculated using the error propagation analysis based on the errors for K_C and B. For some data points, the error bars are within the symbols. Numerical results are shown in Table 1. To see this figure in color, go online.

saturated palmitoyl (16:0) *sn*-1 chain and a monounsaturated oleoyl (18:1) *sn*-2 chain. The measured order parameter profiles with and without DA are shown in Fig. 7. Because the order parameters are highly sensitive to temperature, it is customary to show results over a range of temperatures. Reassuringly, with increasing temperature (from 30°C to 45°C), the order parameters decrease as expected. As commonly seen for saturated lipid chains in lamellar liquid crystalline phases, the order parameters are the highest for carbon segments close to the headgroup region (so-called plateau region) and decrease progressively toward the end of the chain. The order parameters of POPS-d_{31} are higher than those of POPC-d_{31} at all measured temperatures, consistent with literature data (51). As shown in the figure, the presence of DA causes the chains to become more disordered, albeit modestly, in both lipids at all temperatures.

Using a mean-torque model for carbon segment orientations (44), we used the plateau order parameters (carbons 2 to 8) to calculate the cross-sectional area of the palmitoyl (C16:0) chains. These results are shown in Table 3.

We note that DA increases the cross-sectional area of the 16:0 acyl chain similar to the XDS results shown above. Additional information on the effect of DA on lipid structure and dynamics is obtained by EPR spectroscopy, which is shown next.

EPR spectroscopy

We have acquired the EPR spectra for 16-DSA and N-TEMPO probes incorporated into multilamellar vesicles of DOPC, DLPC, and DOPS lipids in the absence and the presence of DA (see supporting material). N-TEMPO measures changes near the lipid headgroup, while 16-DSA measures changes near the bilayer center. We find that DA produces measurable differences in rotational correlation times τ_c that are calculated from the spectra (see Eq. 4), and these results are summarized in Table 4.

As opposed to solid-state ^{2}H NMR, which gives order parameters and therefore information on chain structure, EPR using N-TEMPO gives us a rotational correlation time that we use to estimate local viscosity, which in turn is relevant to the timescale of DA diffusion. We included 16-DSA as a probe on the other end of the lipid to illustrate the difference in dynamics between the headgroup region and membrane interior.

The measured 16-DSA spectra are characteristic of high disorder ($S < 0.2$) near the bottom of the chain, which is treated as approximately isotropic. The rotational correlation times measured are in the nanosecond range, which is the fast tumbling regime, and are comparable to published work (52). The τ_c values are larger (corresponding to higher microviscosity) in DOPS than in DLPC and DOPC and are affected by DA in the same manner. For all three lipids, DA increases the probe's rotational correlation times.

Similar to 16-DSA, the N-TEMPO spectrum is also a high-disorder spectrum and is treated as originating from quasi-isotropic motion near the headgroup region. The measured rotational correlation times are in the fast tumbling regime in the nanosecond timescale, analogous to

TABLE 1 Parameters obtained from x-ray data for DOPC and DLPC for different molar ratios of DA:lipid at 25°C

	DA:lipid	$K_C(10^{-13}$ erg)	$B(10^{12}$erg /cm^4)	D (Å)	$2D_C$ (Å)	D_B (Å)	A (Å^2)	D'_W (Å)
DOPC	0:1	8.8 ± 0.1	10.9 ± 0.1	61.8	26.9	36.0	72.3	14.9
	1:10	7.6 ± 0.1	7.9 ± 0.2	66.7	26.6	36.3	73.0	20.1
	1:3	8.4 ± 0.4	3.4 ± 0.2	70.2	26.1	36.6	74.5	24.1
DLPC	0:1	6.4 ± 0.1	5.9 ± 0.2	59.4	21.4	32.1	61.8	18.0
	1:10	6.3 ± 0.1	4.8 ± 0.2	69.4	21.2	32.5	62.3	28.2
	1:3	6.7 ± 0.9	1.6 ± 0.9	71.3	20.6	32.8	64.2	30.7

Measurements for each lipid/DA composition are from single samples. The error values obtained from the goodness of fit are ±0.5 Å for $2D_C$ and ± 1 Å^2 for A. One noticeable effect of DA on membrane structure is the increase in the area per lipid, and this is plotted in Fig. 5. Addition of DA to either lipid at a molar ratio of 1:3 increases the cross-sectional area per lipid by 2.4 Å^2. (Extrapolation to 1:1 DA/lipid gives 7.2 Å^2 per dopamine molecule.) The increase of cross-sectional area per lipid due to addition of DA is supported by solid-state ^{2}H NMR results (Table 3).

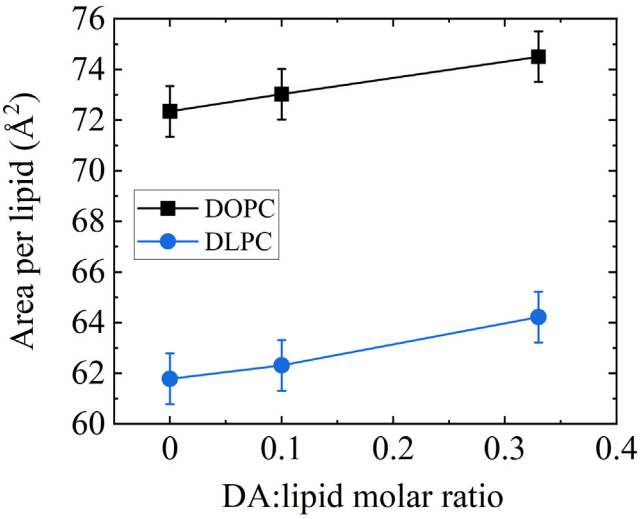

FIGURE 5 The cross-sectional area per lipid versus DA/lipid molar ratio at 25°C obtained using the NFIT program (see materials and methods). To see this figure in color, go online.

published work (53). The measured N-TEMPO rotational correlation times are larger in DOPS than in DOPC and DLPC (in a different order than for 16-DSA). However, adding DA has the same effect on correlation times: for all three lipids, DA causes the rotational correlation time to increase.

A priori, higher disorder would be expected to be accompanied by a shorter correlation time. The difference in timescale for EPR and NMR, a limitation of the assumption that the label motion is isotropic, or a change in depth of the EPR probe in the presence of DA may be responsible for the apparent contradiction posed by our data. That the effect on N-TEMPO is greater indicates, nevertheless, an interfacial interaction for DA.

The changes in rotational correlation times ($\Delta\tau_c$) of 16-DSA and N-TEMPO due to the DA for DOPC, DOPS, and DLPC are shown in Fig. 8. The measured $\Delta\tau_c$ values are in the range of 0–0.1 ns and are more noticeable for N-TEMPO than for 16-DSA. In the case of N-TEMPO, the increase exceeds experimental uncertainty, while in the case of 16-DSA, the increase is comparable or within experimental uncertainty. For both probes, the changes in rotational correlation times increase from DOPC to DOPS to DLPC.

DISCUSSION

There are effectively two orthogonal aspects that have evolved in our study. The first and original aspect is the effect of DA on membrane properties. Such effects would support a mechanism by which DA might perform its biological role by modifying the overall membrane lateral pressure profile to activate membrane proteins without close contact with or binding of the DA (54–56). We do find that DA affects membrane properties: it increases the cross-sectional area per lipid corresponding to decreased acyl chain order parameters, it affects membrane-membrane interactions as indicated by changes in lamellar spacing, and it modifies the molecular dynamics in the lipid headgroup region as measured by the rotational correlation times of EPR probes. Surprisingly, despite the above effects, DA does not seem to affect the membrane bending rigidity K_C. On the whole, however, these changes are not large, especially when one realizes that the concentrations of DA that we studied are very high. The overall DA concentration in the synaptic region is only of the order of 50 nM (57). Even if all this DA became bound to the target axon membrane, the ratio of DA to lipid would be of order 10^{-6} instead of our used ratio of 0.1. Therefore, this putative mechanism does not seem likely to supplant the conventional mechanism of specific binding of DA to a receptor.

The second, more important, aspect of our paper relates to how the membrane could speed up the kinetics of DA signal transduction. Our main result for this aspect is that DA strongly associates with the interfacial region of the membrane. By combining scattering and spectroscopic methods, we have shown that DA has a pronounced affinity to the lipid-water interface. We have shown using XDS that the zwitterionic DA locates in the headgroup region, either near the glycerol-carbonyl region in DOPC or near the phosphate groups in DLPC. EPR confirmed the headgroup location in DOPC, DLPC, and DOPS, while NMR showed only a slight disordering of the acyl chains in POPC and POPS due to DA. This is consistent with previous measurements by solution-state NMR (22) as well as MD simulations (58) that have indicated the preference of DA for the lipid headgroup region. This association of DA with lipid membrane is generally consistent with aromatic moieties having a preference for the lipid headgroup region (32,59) due to dipole interactions between the aromatic groups and lipid headgroups (60,61).

Given this preference, it is plausible that DA undergoes two-dimensional diffusion to its target receptor after being collected and concentrated by the membrane (62,63). Depending upon the appropriate diffusion coefficients, this could be more efficient than the conventional picture of purely three-dimensional diffusion to the membrane receptor. It is known that the lipid matrix provides a quasi-two-dimensional milieu for diffusion of membrane-bound, biological molecules (64–68). These include protein transmembrane domains as well as surface-bound G protein units. It is even more likely that smaller chemical groups, such as DA, located in the membranes would also undergo two-dimensional diffusion within the interfacial headgroup region.

The diffusion of DA in membranes can be estimated based on local viscosity, which is obtained from the rotational correlation times of the EPR probes. Membrane local viscosity η based on a simplified model is given by

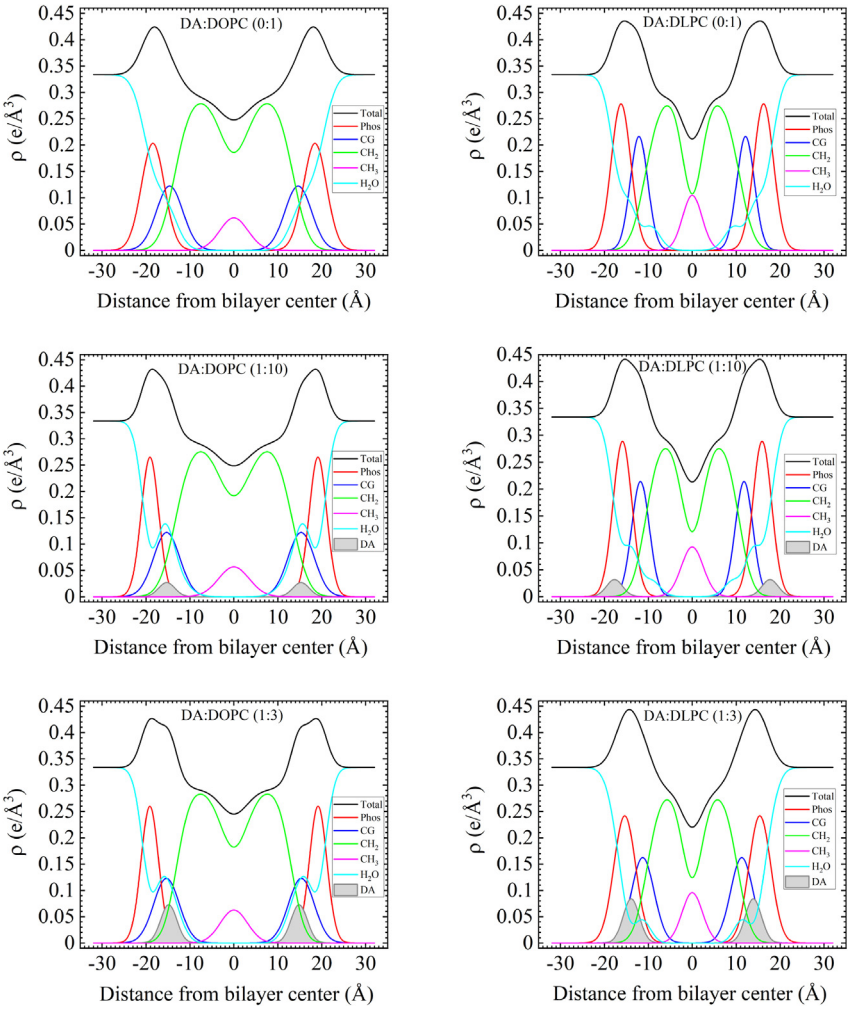

FIGURE 6 Electron density profiles obtained from XDS data at 25°C showing the overall distributions (*black*) as well as various contributions: phosphate (*red*), carbonyl glycerol (*blue*), methylene groups (*green*), methyl groups (*pink*), water (*cyan*), and DA (*shaded gray*). The interfacial water region extends to larger distances as given by $D/2$ in Table 1. To see this figure in color, go online.

$$\eta = \frac{3k_BT\tau_c}{4\pi r^3}, \qquad \text{(Equation 5)}$$

where k_B is Boltzmann constant, T is temperature, and r is the hydrodynamic radius (69–71). Using a heuristic value of $r = 4$ Å at $T = 25°C$, the η values are on the order of $12 - 14$ mPa · s for 16-DSA and $19 - 24$ mPa · s for N-TEMPO. (Using $r = 3$ Å gives us $29 - 33$ mPa · s for 16-DSA and $46 - 58$ mPa · s for N-TEMPO.) To put this range of values in perspective, the dynamic viscosities for water, olive oil, and glycerol at this temperature are ≈ 1, 100, and 1500 mPa · s, respectively.

Using simple diffusion models (72), we estimate the translational diffusion coefficient by

$$D_t = \frac{k_BT}{6\pi\eta r}. \qquad \text{(Equation 6)}$$

Using $r = 4$ Å for DA's radius (volume = 246 Å^3) together with the viscosity of N-TEMPO, the translational diffusion coefficients of DA in the membrane are on order of $2.2 - 2.6 \cdot 10^{-7}$ cm^2 s^{-1}. That gives an estimated mean-travel distance of 0.2 μm in 1 ms, which is the timescale of DA processes in the brain (1,12). Of course, the effective viscosity experienced by DA is likely to be smaller than for the spin-labeled probe because the latter has a long tail that resides in the more viscous hydrocarbon region. If we use the diffusion coefficient ($8.2 \pm 1.3 \cdot 10^{-7}$ cm^2 s^{-1}) that has been reported at the cell surface (11), the mean-travel distance increases by about a factor of two. Also

TABLE 2 D_{peaks} **is the head-to-head distance,** z_{DA} **is the DA average distance from the bilayer center, and** $\Delta z_{DA} = D_{peaks}/2 - z_{DA}$ **is the distance between the headgroup peak and DA**

	DA:lipid	D_{peaks} (Å)	z_{DA} (Å)	Δz_{DA} (Å)
DOPC	0:1	36.1	–	–
	1:10	37.5	15.3	3.5
	1:3	37.6	14.9	3.9
DLPC	0:1	31.0	–	–
	1:10	30.7	17.7	−2.4
	1:3	29.1	13.9	0.7

[2]H NMR spectroscopy.

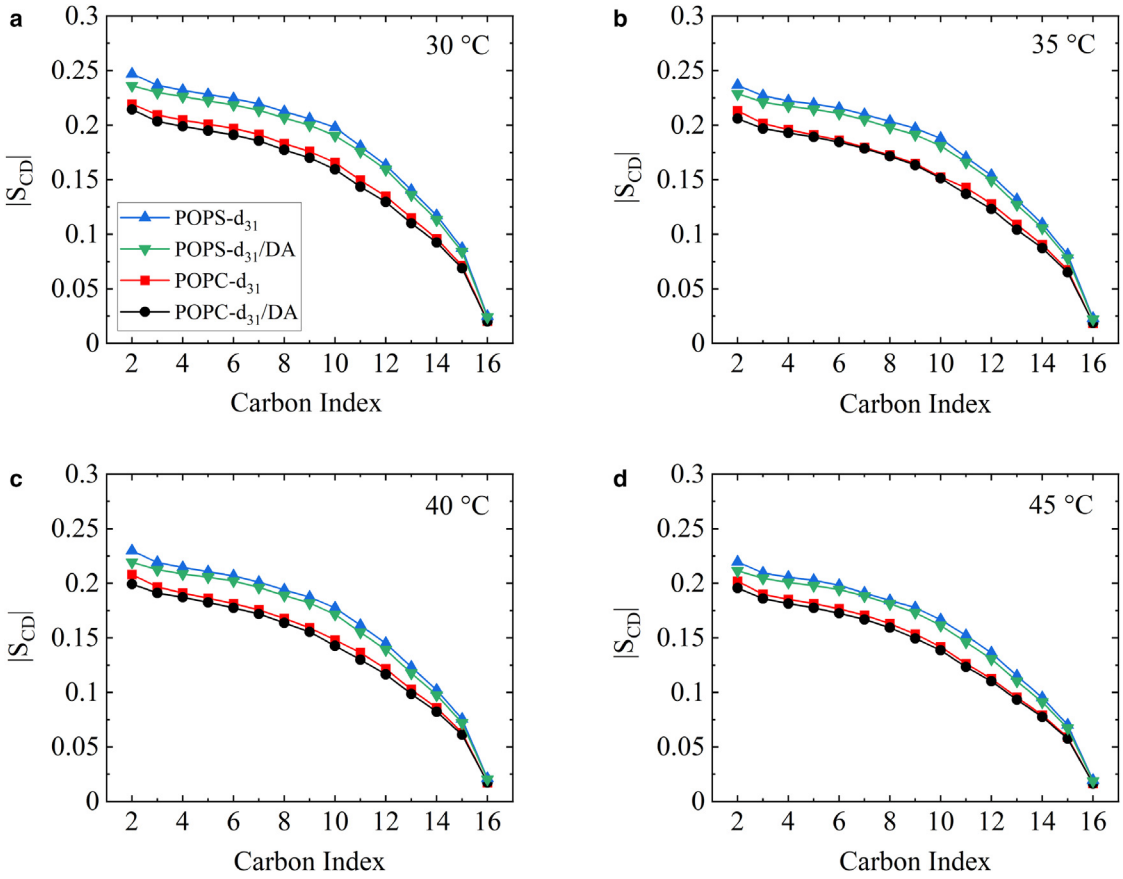

FIGURE 7 Order parameter profiles for POPC-d_{31} and POPS-d_{31} in the absence and the presence of DA. Measurement temperatures were 30°C (*a*), 35°C (*b*), 40°C (*c*), and 45°C (*d*). The molar ratio of DA to lipid is 1:10. Measurements for each lipid/DA composition are from single samples. A reproducibility of ±1% applies to order parameter values. To see this figure in color, go online.

note that since DA does not span the membrane, two-dimensional diffusion models for cylindrical transmembrane inclusions might not apply (64).

It is important to realize, however, that both the cellular membrane and its surroundings are crowded spaces, and therefore the viscosities of both environments are expected to be significantly higher than that of dilute aqueous solutions. Consequently, molecular diffusion in the aqueous space is significantly hindered (73,74). Moreover, while all molecular species in the membrane diffuse concomitantly, they would do so at different rates (72,75–78). In particular, a small molecule like DA, residing in the interfacial region composed of a nearly equal concentration of highly mobile lipid headgroups and water, would diffuse laterally much faster than lipids themselves. Furthermore, the dynamics (translation and rotation) of receptors themselves can affect the probability of ligand-receptor encounter. Notably, the question of concomitant diffusion of ligand and receptors is receiving attention in applied mathematical research (79–81).

Moreover, mathematical models of diffusion have shown the marked effect of the number of dimensions in which the

TABLE 3 Average order parameter in the plateau region (carbons 2 to 8) $|\overline{S}_{pl}|$ and cross-sectional area (in units of Å^2) per palmitoyl chain $A_{16:0}$ of POPC-d_{31} and POPS-d_{31} in the absence and the presence of DA at different temperatures

	POPC-d_{31}		POPC-d_{31}/DA		POPS-d_{31}		POPS-d_{31}/DA	
Temperature (°C)	$\lvert\overline{S}_{pl}\rvert$	$A_{16:0}$	$\lvert\overline{S}_{pl}\rvert$	$A_{16:0}$	$\lvert\overline{S}_{pl}\rvert$	$A_{16:0}$	$\lvert\overline{S}_{pl}\rvert$	$A_{16:0}$
30	0.201	30.74	0.195	31.11	0.229	29.16	0.222	29.53
35	0.191	31.55	0.188	31.75	0.219	29.86	0.214	30.14
40	0.187	32.00	0.182	32.35	0.211	30.49	0.205	30.84
45	0.181	32.61	0.177	32.92	0.202	31.22	0.197	31.53

The molar ratio of DA to lipid is 1:10. Measurements for each lipid/DA composition are from single samples. A reproducibility of ±1% applies to $|\overline{S}_{pl}|$ values.

TABLE 4 EPR rotational correlation times of 16-DSA and N-TEMPO obtained from the EPR spectra at 25°C

Sample	τ_c (16-DSA) (ns)	τ_c (N-TEMPO) (ns)
DOPC	0.809 ± 0.012	1.329 ± 0.014
DOPC/DA	0.813 ± 0.009	1.358 ± 0.004
DLPC	0.857 ± 0.026	1.256 ± 0.036
DLPC/DA	0.880 ± 0.009	1.348 ± 0.027
DOPS	0.885 ± 0.002	1.521 ± 0.040
DOPS/DA	0.898 ± 0.013	1.591 ± 0.011

The molar ratio of DA to lipid and 16-DSA is 10:100:1, and the molar ratio of DA to lipid and N-TEMPO is 50:500:1. The values for τ_c are an average of three measurements, and the uncertainty is the standard deviation from the mean. For all cases but N-TEMPO with DOPS with and without DA, measurements were performed on single samples and repeated three times. All three measurements were run within 24 h after making the samples. For N-TEMPO with DOPS with and without DA, three separate samples were measured. The error values indicate standard deviations from the mean.

molecular motion takes place as well as the influence of the space topology with two-dimensional diffusion being an important case (65,82). It is conceivable that two-dimensional diffusion in the lipid matrix could play an important role for the encounter of neuromodulators and their membrane receptors (13,62,79,81). Supposing that a quasi-equilibrium is established after initial release of DA from the presynaptic neuron, then the concentration of DA within the target membrane will be much higher than the concentration in water. This provides a reservoir of membrane DA that could be more likely to find target receptors via two-dimensional diffusion than a dilute aqueous concentration of DA undergoing three-dimensional diffusion.

We therefore suggest that the primary pathway for DA signal transduction is diffusion along the lipid membrane headgroup region until it meets its receptor. This hypothesis implies that the lipid composition of the target membrane can affect the timescale of DA action, as has been reported (19–21). Furthermore, although the location of DA binding sites on receptors is not entirely clear (18,83–85), the receptors may have evolved DA binding sites that are themselves buried in the membrane and are therefore less accessible to binding DA from solution. On the other hand, even if the receptor binding site is in the aqueous phase, the off rate of DA from the headgroup region would still allow the final contact with the reception binding site.

When working with multilamellar samples, there is always the question whether the added molecular species (such as DA in this case) is excluded or not from the interlamellar space. This is important because if DA was excluded into an excess water phase, then the effects we measure would be primarily osmotic as opposed to specific interactions with the lipids (86,87). One of the best indicators of osmotic effects is the lamellar repeat spacing: if D decreases with the additive, it strongly indicates that the additive is excluded from the multilamellar structure and acts osmotically within an excess water phase. However, we found that the D-spacing increases; this indicates that the added molecular species enters the multilamellar lipid structure, where it can either reside in the interlamellar water region, in the membrane, or in both.

It should be noted that the choice of lipids in our studies depended on two factors: 1) the limitations of each experimental method and 2) prior studies. For example, while solid-state ^{2}H NMR spectroscopy can, in principle, be done on any deuterated lipid, the assignment to carbon segments is not easily done for unsaturated chains. For this reason, we opted for deuterated POPC and POPS lipids, which have been extensively used in ^{2}H NMR spectroscopy. In contrast, measurements of membrane interactions on DLPC and DOPC membranes by other techniques are relatively more common.

Regarding interbilayer interactions, we note that the equilibrium D-spacings for DLPC and DOPC in water are very different, as expected based on different interaction parameters, especially K_C. Our current K_C values agree well with previous measurements. Previous measurements reported $K_C = 8 \cdot 10^{-13}$ erg at 63.3 Å for DOPC (88) and $K_C = 5.5 \cdot 10^{-13}$ erg at 61.1 Å for DLPC (39). Interestingly, when DA is added, the B versus D data tend to follow the same curve at larger values of D. One possible explanation is that at these distances, the balance of intermembrane interactions is primarily between the van der Waals attraction and the electrostatic repulsion caused by the DA molecules associated with the lipid headgroups and is enhanced by the fluctuation term. This particular balance of interlamellar

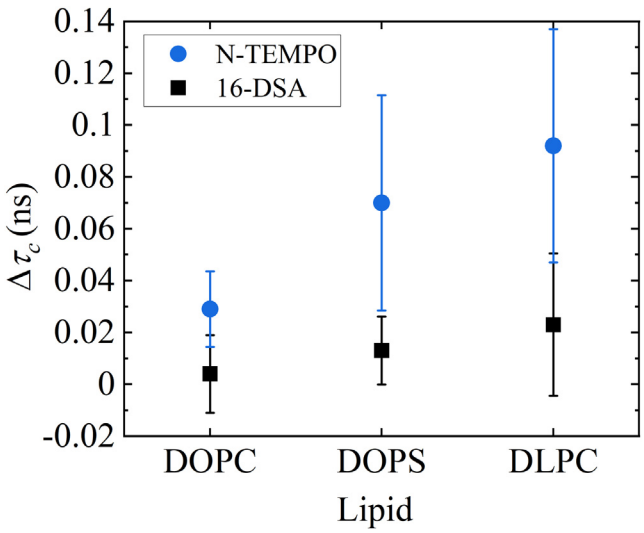

FIGURE 8 The changes in rotational correlation times of 16-DSA and N-TEMPO probes due to the DA for DOPC, DOPS, and DLPC at 25°C. The molar ratio of DA to lipid and 16-DSA is 10:100:1, and the molar ratio of DA to lipid and N-TEMPO is 50:500:1. For all cases but N-TEMPO with DOPS with and without DA, measurements were performed on single samples and repeated three times. All three measurements were run within 24 h after making the samples. For N-TEMPO with DOPS with and without DA, three separate samples were measured. The error bars indicate standard deviations from the mean. To see this figure in color, go online.

forces leads to swelling curves similar to those measured in the presence of KBr salt. In the case of KBr solutions, it has been shown that the electrostatic repulsion due to Br^- binding to PC headgroups fully explains the observed multilamellar swelling (32,33). Our results in Fig. 2 indicate that a similar mechanism occurs in the case of DA as well. This swelling of lipid multilayers is accompanied by large changes in the B parameters and a significant effect of DA on the amplitude of membrane shape fluctuations: in the presence of DA, the ratios of σ to D and to D_W are $\sigma/D \approx 10\%$ and $\sigma/D_W \approx 18\%$.

DA location and dynamics are also expected to be affected by pH, salt, and lipid membrane composition. Our report using simplified lipid systems provides an experimental baseline for DA-lipid membrane interactions, which can be used for further development of molecular modeling of DA dynamics and its probability of encounter with its receptors.

CONCLUSIONS

We find that DA is strongly associated with the interfacial lipid headgroup region of lipid bilayers compared with either the hydrocarbon region or the aqueous region. We suggest that DA released in the brain is collected by target membranes in order to provide, via two-dimensional diffusion along the membrane, more efficient encounter with its receptors.

SUPPORTING MATERIAL

Supporting material can be found online at https://doi.org/10.1016/j.bpj.2023.02.016.

AUTHOR CONTRIBUTIONS

A.S. prepared samples, performed measurements, analyzed data, and wrote the manuscript. S.M., S.R.W., and S.T.-N. analyzed data and wrote the manuscript. J.F.N. performed measurements and wrote the manuscript. H.I.P. designed project, analyzed data, and wrote the manuscript.

ACKNOWLEDGMENTS

The authors would like to thank Klaus Gawrisch for his sustained and innovative contribution to biophysics. H.I.P. is grateful for Klaus Gawrisch's mentorship at the NIH and for the many engaging and entertaining conversations. S.T.-N. and J.F.N. thank Klaus for many meaningful discussions and complementary experiments. A.S. thanks the Physics Department at IUPUI for the Fellowship Award. S.T.-N. and S.M. acknowledge support from National Science Foundation (NSF) MCB-2115790.

DECLARATION OF INTERESTS

The authors declare no competing interests.

REFERENCES

1. Liu, C., P. Goel, and P. S. Kaeser. 2021. Spatial and temporal scales of dopamine transmission. *Nat. Rev. Neurosci.* 22:345–358.
2. Jodko-Piorecka, K., and G. Litwinienko. 2013. First experimental evidence of dopamine interactions with negatively charged model biomembranes. *ACS Chem. Neurosci.* 4:1114–1122.
3. Iversen, S. D., and L. L. Iversen. 2007. Dopamine: 50 years in perspective. *Trends Neurosci.* 30:188–193.
4. Wang, D., Y. Peng, …, D. Tang. 2016. Antiferroptotic activity of non-oxidative dopamine. *Biochem. Biophys. Res. Commun.* 480:602–607.
5. Cheng, M. H., and I. Bahar. 2015. Molecular mechanism of dopamine transport by human dopamine transporter. *Structure.* 23:2171–2181.
6. Gedeon, P. C., M. Indarte, …, J. D. Madura. 2010. Molecular dynamics of leucine and dopamine transporter proteins in a model cell membrane lipid bilayer. *Proteins.* 78:797–811.
7. Durdagi, S., R. E. Salmas, …, P. Seeman. 2016. Binding interactions of dopamine and apomorphine in D2High and D2Low states of human dopamine D2 receptor using computational and experimental techniques. *ACS Chem. Neurosci.* 7:185–195.
8. Silwal, A. P., R. Yadav, …, H. P. Lu. 2017. Raman spectroscopic signature markers of dopamine–human dopamine transporter interaction in living cells. *ACS Chem. Neurosci.* 8:1510–1518.
9. Yuan, Y., J. Zhu, and C.-G. Zhan. 2018. Flipped phenyl ring orientations of dopamine binding with human and drosophila dopamine transporters: remarkable role of three nonconserved residues. *ACS Chem. Neurosci.* 9:1426–1431.
10. Zhan, D., S. Mao, …, Y. Shao. 2004. Electrochemical investigation of dopamine at the water/1, 2-dichloroethane interface. *Anal. Chem.* 76:4128–4136.
11. Trouillon, R., Y. Lin, …, A. G. Ewing. 2013. Evaluating the diffusion coefficient of dopamine at the cell surface during amperometric detection: disk vs ring microelectrodes. *Anal. Chem.* 85:6421–6428.
12. Liu, C., and P. S. Kaeser. 2019. Mechanisms and regulation of dopamine release. *Curr. Opin. Neurobiol.* 57:46–53.
13. Rusakov, D. A., L. P. Savtchenko, …, J. M. Henley. 2011. Shaping the synaptic signal: molecular mobility inside and outside the cleft. *Trends Neurosci.* 34:359–369.
14. Mei, N., M. Robinson, …, Z. Leonenko. 2020. Melatonin alters fluid phase coexistence in POPC/DPPC/cholesterol membranes. *Biophys. J.* 119:2391–2402.
15. Peters, G. H., C. Wang, …, P. Westh. 2013. Binding of serotonin to lipid membranes. *J. Am. Chem. Soc.* 135:2164–2171.
16. Engberg, O., A. Bochicchio, …, D. Huster. 2020. Serotonin alters the phase equilibrium of a ternary mixture of phospholipids and cholesterol. *Front. Physiol.* 11:578868.
17. Dey, S., D. Surendran, …, S. Maiti. 2021. Altered membrane mechanics provides a receptor-independent pathway for serotonin action. *Chemistry.* 27:7533–7541.
18. Postila, P. A., I. Vattulainen, and T. Róg. 2016. Selective effect of cell membrane on synaptic neurotransmission. *Sci. Rep.* 6:19345.
19. Yang, Z., L. Gou, …, L. Zhang. 2017. Membrane fusion involved in neurotransmission: glimpse from electron microscope and molecular simulation. *Front. Mol. Neurosci.* 10:168. https://www.frontiersin.org/article/10.3389/fnmol.2017.00168.
20. Lauwers, E., R. Goodchild, and P. Verstreken. 2016. Membrane lipids in presynaptic function and disease. *Neuron.* 90:11–25. https://www.sciencedirect.com/science/article/pii/S0896627316001707.
21. Biswas, B., and P. C. Singh. 2021. Restructuring of membrane water and phospholipids in direct interaction of neurotransmitters with model membranes associated with synaptic signaling: interface-selective vibrational sum frequency generation study. *J. Phys. Chem. Lett.* 12:2871–2879.
22. Matam, Y., B. D. Ray, and H. I. Petrache. 2016. Direct affinity of dopamine to lipid membranes investigated by Nuclear Magnetic Resonance spectroscopy. *Neurosci. Lett.* 618:104–109.

23. Biswas, B., and P. C. Singh. 2022. Protonation state of dopamine neurotransmitter at the aqueous interface: vibrational sum frequency generation spectroscopy study. *Langmuir.* 38:1380–1385.
24. Jodko-Piorecka, K., B. Sikora, …, G. Litwinienko. 2021. Antiradical activity of dopamine, L-DOPA, adrenaline, and noradrenaline in water/methanol and in liposomal systems. *J. Org. Chem.*
25. Bavi, O., C. D. Cox, …, B. Martinac. 2016. Influence of global and local membrane curvature on mechanosensitive ion channels: a finite element approach. *Membranes.* 6:14.
26. Peeters, B. W. A., A. C. A. Piët, and M. Fornerod. 2022. Generating membrane curvature at the nuclear pore: a lipid point of view. *Cells.* 11:469.
27. McMahon, H. T., M. M. Kozlov, and S. Martens. 2010. Membrane curvature in synaptic vesicle fusion and beyond. *Cell.* 140:601–605.
28. Dhara, M., M. Mantero Martinez, …, D. Bruns. 2020. Synergistic actions of v-SNARE transmembrane domains and membrane-curvature modifying lipids in neurotransmitter release. *Elife.* 9:e55152.
29. McMahon, H. T., and E. Boucrot. 2015. Membrane curvature at a glance. *J. Cell Sci.* 128:1065–1070.
30. Petrache, H. I., N. Gouliaev, …, J. F. Nagle. 1998. Interbilayer interactions from high-resolution x-ray scattering. *Phys. Rev. E.* 57:7014–7024.
31. Petrache, H. I., S. Tristram-Nagle, …, V. A. Parsegian. 2006. Swelling of phospholipids by monovalent salt. *J. Lipid Res.* 47:302–309.
32. Koerner, M. M., L. A. Palacio, …, H. I. Petrache. 2011. Electrodynamics of lipid membrane interactions in the presence of zwitterionic buffers. *Biophys. J.* 101:362–369.
33. Petrache, H. I., T. Zemb, …, V. A. Parsegian. 2006. Salt screening and specific ion adsorption determine neutral-lipid membrane interactions. *Proc. Natl. Acad. Sci. USA.* 103:7982–7987.
34. Tristram-Nagle, S., R. Zhang, …, J. F. Nagle. 1993. Measurement of chain tilt angle in fully hydrated bilayers of gel phase lecithins. *Biophys. J.* 64:1097–1109.
35. Tristram-Nagle, S. A. 2007. Preparation of oriented, fully hydrated lipid samples for structure determination using X-ray scattering. *Methods Mol. Biol.* 400:63–75.
36. Lyatskaya, Y., Y. Liu, …, J. F. Nagle. 2001. Method for obtaining structure and interactions from oriented lipid bilayers. *Phys. Rev. E Stat. Nonlin. Soft Matter Phys.* 63:011907.
37. Liu, Y. 2003. New Method to Obtain Structure of Biomembranes Using Diffuse X-Ray Scattering: Application to Fluid Phase DOPC Lipid Bilayers. Carnegie Mellon University, Ph.D. thesis.
38. Liu, Y., and J. F. Nagle. 2004. Diffuse scattering provides material parameters and electron density profiles of biomembranes. *Phys. Rev. E Stat. Nonlin. Soft Matter Phys.* 69:040901.
39. Kučerka, N., Y. Liu, …, J. F. Nagle. 2005. Structure of fully hydrated fluid phase DMPC and DLPC lipid bilayers using X-ray scattering from oriented multilamellar arrays and from unilamellar vesicles. *Biophys. J.* 88:2626–2637.
40. Kinnun, J. J., R. Bittman, …, S. R. Wassall. 2018. DHA modifies the size and composition of raftlike domains: a solid-state 2H NMR study. *Biophys. J.* 114:380–391.
41. Sternin, E. 1985. Data acquisition and processing: a systems approach. *Rev. Sci. Instrum.* 56:2043–2049.
42. Davis, J., K. Jeffrey, …, T. Higgs. 1976. Quadrupolar echo deuteron magnetic resonance spectroscopy in ordered hydrocarbon chains. *Chem. Phys. Lett.* 42:390–394.
43. Seelig, J. 1977. Deuterium magnetic resonance: theory and application to lipid membranes. *Q. Rev. Biophys.* 10:353–418.
44. Petrache, H. I., S. W. Dodd, and M. F. Brown. 2000. Area per lipid and acyl length distributions in fluid phosphatidylcholines determined by 2H NMR spectroscopy. *Biophys. J.* 79:3172–3192.
45. Mallikarjunaiah, K. J., J. J. Kinnun, …, M. F. Brown. 2019. Flexible lipid nanomaterials studied by NMR spectroscopy. *Phys. Chem. Chem. Phys.* 21:18422–18457.
46. Molugu, T. R., X. Xu, …, M. F. Brown. 2018. Solid-state 2 H NMR studies of water-mediated lipid membrane deformation. *In* Modern Magnetic Resonance. G. Webb, ed Springer:1–27.
47. Eletr, S., and G. Inesi. 1972. Phase changes in the lipid moieties of sarcoplasmic reticulum membranes induced by temperature and protein conformation changes. *Biochim. Biophys. Acta.* 290:178–185.
48. Keith, A., G. Bulfield, and W. Snipes. 1970. Spin-labeled neurospora mitochondria. *Biophys. J.* 10:618–629.
49. Rawicz, W., K. C. Olbrich, …, E. Evans. 2000. Effect of chain length and unsaturation on elasticity of lipid bilayers. *Biophys. J.* 79:328–339.
50. Nagle, J. F., and S. Tristram-Nagle. 2000. Structure of lipid bilayers. *Biochim. Biophys. Acta.* 1469:159–195.
51. Justice, M. J., D. N. Petrusca, …, H. I. Petrache. 2014. Effects of lipid interactions on model vesicle engulfment by alveolar macrophages. *Biophys. J.* 106:598–609.
52. Wassall, S. R., R. C. McCabe, …, W. Stillwell. 1992. Effects of dietary fish oil on plasma high density lipoprotein. Electron spin resonance and fluorescence polarization studies of lipid ordering and dynamics. *J. Biol. Chem.* 267:8168–8174.
53. Ghiasi, F., M. H. Eskandari, …, F. Ortega. 2021. Build-up of a 3D organogel network within the bilayer shell of nanoliposomes. A novel delivery system for vitamin D3: preparation, characterization, and physicochemical stability. *J. Agric. Food Chem.* 69:2585–2594.
54. Cantor, R. S. 1999. Lipid composition and the lateral pressure profile in bilayers. *Biophys. J.* 76:2625–2639.
55. Bezrukov, S. M. 2000. Functional consequences of lipid packing stress. *Curr. Opin. Colloid Interface Sci.* 5:237–243.
56. Josey, B. P., F. Heinrich, …, M. Lösche. 2020. Association of model neurotransmitters with lipid bilayer membranes. *Biophys. J.* 118:1044–1057.
57. Ross, S. B. 1991. Synaptic concentration of dopamine in the mouse striatum in relationship to the kinetic properties of the dopamine receptors and uptake mechanism. *J. Neurochem.* 56:22–29.
58. Lolicato, F., H. Juhola, …, T. Róg. 2020. Membrane-dependent binding and entry mechanism of dopamine into its receptor. *ACS Chem. Neurosci.* 11:1914–1924.
59. Johnson, M. A., B. D. Ray, …, H. I. Petrache. 2015. Equivalent isopropanol concentrations of aromatic amino acids interactions with lipid vesicles. *J. Membr. Biol.* 248:695–703.
60. Yau, W.-M., W. C. Wimley, …, S. H. White. 1998. The preference of tryptophan for membrane interfaces. *Biochemistry.* 37:14713–14718.
61. Sun, H., D. V. Greathouse, …, R. E. Koeppe. 2008. The preference of tryptophan for membrane interfaces: insights from N-methylation of tryptophans in gramicidin channels. *J. Biol. Chem.* 283:22233–22243.
62. Savtchenko, L. P., S. M. Korogod, and D. A. Rusakov. 2000. Electrodiffusion of synaptic receptors: a mechanism to modify synaptic efficacy? *Synapse.* 35:26–38.
63. Postila, P. A., and T. Róg. 2020. A perspective: active role of lipids in neurotransmitter dynamics. *Mol. Neurobiol.* 57:910–925.
64. Saffman, P. G., and M. Delbrück. 1975. Brownian motion in biological membranes. *Proc. Natl. Acad. Sci. USA.* 72:3111–3113.
65. Saxton, M. J. 1993. Lateral diffusion in an archipelago. Dependence on tracer size. *Biophys. J.* 64:1053–1062.
66. Stollberg, J. 1995. Density and diffusion limited aggregation in membranes. *Bull. Math. Biol.* 57:651–677.
67. Melo, E., and J. Martins. 2006. Kinetics of bimolecular reactions in model bilayers and biological membranes. A critical review. *Biophys. Chem.* 123:77–94.
68. Saxton, M. J. 2007. Modeling 2D and 3D diffusion. *Methods Mol. Biol.* 400:295–321.
69. Mladenova, B. Y., N. A. Chumakova, …, D. R. Kattnig. 2012. Rotational and translational diffusion of spin probes in room-temperature ionic liquids. *J. Phys. Chem. B.* 116:12295–12305.
70. Fraissard, J., and O. Lapina. 2012. Magnetic Resonance in Colloid and Interface Science, volume 76. Springer Science & Business Media.

71. Sengupta, A., and K. Rm. 2016. Electron paramagnetic resonance spectroscopic investigation of the dynamics of spin probe in room temperature ionic liquid. *Mod. Chem. Appl.* 04:1000189.

72. Li, C., Y. Wang, and G. J. Pielak. 2009. Translational and rotational diffusion of a small globular protein under crowded conditions. *J. Phys. Chem. B.* 113:13390–13392.

73. Zheng, K., T. P. Jensen, …, D. A. Rusakov. 2017. Nanoscale diffusion in the synaptic cleft and beyond measured with time-resolved fluorescence anisotropy imaging. *Sci. Rep.* 7:42022.

74. Nicholson, C., and S. Hrabětová. 2017. Brain extracellular space: the final frontier of neuroscience. *Biophys. J.* 113:2133–2142.

75. Wassall, S. R. 1996. Pulsed field gradient-spin echo NMR studies of water diffusion in a phospholipid model membrane. *Biophys. J.* 71:2724–2732.

76. Orädd, G., and G. Lindblom. 2004. NMR Studies of lipid lateral diffusion in the DMPC/gramicidin D/water system: peptide aggregation and obstruction effects. *Biophys. J.* 87:980–987.

77. Klauda, J. B., M. F. Roberts, …, R. W. Pastor. 2008. Rotation of lipids in membranes: molecular dynamics simulation, 31P spin-lattice relaxation, and rigid-body dynamics. *Biophys. J.* 94:3074–3083.

78. Macdonald, P. M., Q. Saleem, …, H. H. Morales. 2013. NMR methods for measuring lateral diffusion in membranes. *Chem. Phys. Lipids.* 166:31–44.

79. Savtchenko, L. P., M. M. Poo, and D. A. Rusakov. 2017. Electrodiffusion phenomena in neuroscience: a neglected companion. *Nat. Rev. Neurosci.* 18:598–612.

80. Lawley, S. D., and C. E. Miles. 2019. How receptor surface diffusion and cell rotation increase association rates. *SIAM J. Appl. Math.* 79:1124–1146.

81. Lagache, T., K. Jayant, and R. Yuste. 2019. Electrodiffusion models of synaptic potentials in dendritic spines. *J. Comput. Neurosci.* 47:77–89.

82. Fischer, T., H. J. Risselada, and R. L. C. Vink. 2012. Membrane lateral structure: the influence of immobilized particles on domain size. *Phys. Chem. Chem. Phys.* 14:14500–14508.

83. Kalani, M. Y. S., N. Vaidehi, …, W. A. Goddard, III. 2004. The predicted 3D structure of the human D2 dopamine receptor and the binding site and binding affinities for agonists and antagonists. *Proc. Natl. Acad. Sci. USA.* 101:3815–3820.

84. Zhang, J., B. Xiong, …, A. Zhang. 2009. Dopamine D1 receptor ligands: where are we now and where are we going. *Med. Res. Rev.* 29:272–294.

85. Rondou, P., G. Haegeman, and K. Van Craenenbroeck. 2010. The dopamine D4 receptor: biochemical and signalling properties. *Cell. Mol. Life Sci.* 67:1971–1986.

86. Sukenik, S., S. Dunsky, …, D. Harries. 2017. TMAO mediates effective attraction between lipid membranes by partitioning unevenly between bulk and lipid domains. *Phys. Chem. Chem. Phys.* 19:29862–29871.

87. Sukenik, S., S. Dunsky, …, D. Harries. 2019. How osmolytes modulate lipid interactions. *Biophys. J.* 116:318a.

88. Kučerka, N., S. Tristram-Nagle, and J. F. Nagle. 2005. Structure of fully hydrated fluid phase lipid bilayers with monounsaturated chains. *J. Membr. Biol.* 208:193–202.